Simultaneous and Constrained Calibration of Multiple Hyperspectral Images Through a New Generalized Empirical Line Model

Fadi Kizel, *Member, IEEE*, Jón Atli Benediktsson, *Fellow, IEEE*, Lorenzo Bruzzone, *Fellow, IEEE*, Gro B. M. Pedersen, Olga K. Vilmundardóttir, and Nicola Falco, *Member, IEEE*

***Abstract*—The *empirical line* (EL) calibration method is commonly used for atmospheric correction of remotely sensed spectral images and recovery of surface reflectance. The current EL-based methods are applicable to calibrate only single images. Therefore, the use of the EL calibration is impractical for imaging campaigns, where many (partially overlapped) images are acquired to cover a large area. In addition, the EL results are unconstrained and an undesired reflectance with negative values or larger than 100% can be obtained. In this paper, we use the standard EL model to formulate a new *generalized empirical line* (GEL) model. Based on the GEL, we present a novel method for simultaneous and constrained calibration of multiple images. This new method allows for calibration through *multiple image constrained empirical line* (MIcEL) and three additional calibration modes. Given a set of images, we use the available ground targets and automatically extracted tie points between overlapping images to calibrate all the images in the set simultaneously. Quantitative and visual assessments of the proposed method were carried out relatively to the off-the-shelf method *quick atmospheric correction* (QUAC), using real hyperspectral images and field measurements. The results clearly show the superiority of MIcEL with respect to the minimization of the difference between the reflectance values of the same object in different overlapping images. An assessment of the absolute accuracy, with respect to 11 field measurement points, shows that the accuracy of MIcEL, with an average *mean absolute error* (MAE) of ∼11%, is comparable with respect to the QUAC.**

***Index Terms*—Airborne remote sensing, constrained empirical line calibration, hyperspectral imaging, radiometric calibration, surface reflectance.**

Manuscript received September 30, 2017; revised December 1, 2017; accepted January 24, 2018. Date of publication May 1, 2018; date of current version June 29, 2018. *(Corresponding author: Fadi Kizel.)*

F. Kizel and J. A. Benediktsson are with the Faculty of Electrical and Computer Engineering, University of Iceland, Reykjavík 101, Iceland (e-mail: fadikizel@hi.is; benedikt@hi.is).

L. Bruzzone is with the Department of Information Engineering and Computer Science, University of Trento, Trento 38122, Italy (e-mail: lorenzo.bruzzone@ing.unitn.it).

G. B. M. Pedersen is with the Institute of Earth Science, University of Iceland, Reykjavik 101, Iceland (e-mail: gro@hi.is).

O. K. Vilmundardóttir is with the Institute of Life and Environmental Sciences, University of Iceland, Reykjavik 101, Iceland (e-mail: olgakolbrun@hi.is).

N. Falco is with the Climate & Ecosystem Sciences, Lawrence Berkeley National Laboratory, Berkeley, CA 94720 USA (e-mail: nicolafalco@lbl.gov).

Color versions of one or more of the figures in this paper are available online at http://ieeexplore.ieee.org.

Digital Object Identifier 10.1109/JSTARS.2018.2804666

I. Introduction

RECOVERY of surface reflectance is essential for the reliable analysis of spectral data [1]. At-sensor raw spectral measurements are usually recorded as unit-less *digital number* (DN) or physical units of radiance, e.g., watt per meter per steradian per nanometer ($W \cdot m^{-2} \cdot sr^{-1} \cdot nm^{-1}$) [2]. Both DN and radiance values provide significant spectral information about the measured objects. However, these units are highly affected by a variety of acquisition conditions, which are related to atmospheric effects. In addition, the obtained measurements are affected, to a certain extent, by the *bidirectional reflectance distribution function* (BRDF) effect [3], [4] due to the viewing geometry and anisotropic reflection [5]–[7]. Because of these effects, measurement of the same area under different conditions leads to inconsistent radiometric information which bears inaccuracy in a diversity of spectral applications, e.g., classification [8], [9], unmixing [10], [11], and change detection [12], [13]. To obtain near-invariant spectral measurements, a calibration preprocessing is required to convert the data into surface reflectance units. A variety of methods for surface reflectance retrieval and atmospheric correction have been developed (see [14] for details). One group of methods includes approaches that are based on a *radiative-transfer model* (RTM), e.g., *moderate resolution atmospheric transmission* (MODTRAN) [15], *fast Line-of-sight atmospheric analysis of hypercubes* (FLAASH) [16], and the *atmospheric and topographic correction* (ATCOR) [17]. RTM-based methods are assumed to provide accurate results; however, they are time consuming, complex, and require additional information (and different inputs) to be applied. In many cases, such information is not available and these type of methods cannot be used. On the other hand, in-scene approaches [18], [19] retrieve the surface reflectance using only the image spectral information. In-scene methods are simple to implement but usually provide poor accuracy. However, the *quick atmospheric correction* (QUAC) [20], an improved method based on the in-scene approach, provides accurate results with an absolute accuracy of ∼15% with respect to FLAASH [21]. In practice, QUAC is partially in-scene and its implementation relies on the image spectral information and a spectral library of typical materials that probably exist in natural scenes. QUAC does not require any metadata, and the only requirement is an approximate specification of sensor band locations (i.e., central

wavelengths) and their radiometric calibration [20], [21]. In addition, since first principles radiative-transfer calculations are not needed, QUAC performs significantly faster than physics-based methods. However, a main drawback of the QUAC is that the obtained results are unscaled. Particularly, the estimated spectral signatures have true general shape but multiplied by a certain factor. Thus, the reflectance profile of at least one pixel is needed to estimate the scale factor for each calibrated image. While in-scene and RTM-based methods do not involve any field measurements in the process, ground targets have proven practical for reflectance retrieval, especially for Airborne imagery, in both terms of running time and accuracy [22]–[24]. In this regard, vicarious calibration methods [25] make use of invariant targets for postlaunch calibration of sensors and retrieval of surface reflectance. Both natural [26], [27] and artificial [28], [29] targets were used in previous works. Usually, the ground targets are selected or designed according to the special requirements of the imaging campaign [30]. A simplified and one of the most useful ground target-based methods is the empirical line (EL) [22]. EL calibration relies on the rational assumption that the relationship between raw measurements and surface reflectance can be empirically modeled [31], [32]. Assuming a uniform atmospheric acquisition effects across the image, EL methods estimate the parameters of a specific model using the reflectance values of ground targets in the image [27], [33], [34]. The reflectance of ground targets can be obtained by laboratory or field measurement. However, field measurements at the same time of the image acquisition are preferred. The estimated parameters of the selected model are then used to convert the recorded DN values into reflectance for all the pixels in the image. A linear model [22], which combines two parameters of slope and intercept, is commonly used for this purpose. The ordinary EL method is very useful, especially for its simple implementation. However, the basic formulation of the EL is limited and suitable only for calibration of a single image. To minimize these limitations and improve the obtained results, several significant drawbacks of the EL model need to be considered.

1) There are no constraints on the obtained reflectance and pixels with negative or higher than 100% values are probable.
2) For imaging campaigns of large areas, the spatial consistency of the information is necessary for a mosaic of several scenes into one large image. In practice, it can be impossible to distribute ground targets within each image and the separate calibration of individual images is impractical.
3) Different images are likely to have been acquired under different conditions and thereby the same objects can obtain different reflectance values in different images. Therefore, the estimated calibration coefficients of one image are not suitable for the calibration of other images.

To provide reliable data for spatiotemporal analysis, we need to overcome the above three main gaps while considering the calibration process. To the best of our knowledge, the option of applying constraints on the retrieved reflectance values of the EL has never been addressed in previous works. Moreover, very few works have addressed the simultaneous EL calibration of overlapping images [24], [35]. Furthermore, these methods consider cases for multispectral data but not hyperspectral data. The calibration model in [35] combines relative coefficients (between overlapping images) and absolute coefficients (that convert *DN* into reflectance). This combination, between two types of coefficients, increases the number of unnecessary unknowns (relative coefficients) and the complexity of the problem due to the nonlinearity of the equation system. In [24], the relative offset between overlapping images is minimized using a model that estimates also a single BRDF factor for each image. The model is complex and seven of its parameters are adjusted manually, which reduces the efficiency of the algorithm significantly. Combining the BRDF in the model is theoretically important. However, the results (see [24, Fig. 7]) suggest that the most significant reduction of the difference, between values of the same objects in neighbor images, is achieved only when overlap constraints are applied. Both the works in [24] and [35] contribute to the solution of simultaneous calibration of multiple overlapping images. However, they are applied to a large number of images, but with only four bands. Moreover, the applied models are nonlinear, complex, and do not include any constraints on the obtained reflectance values. Instead, we suggest a simple model that combines only linear equations and constraints to estimate the absolute calibration coefficients of each image directly. Our method involves only first-order derivatives and requires a minimal number of the needed equations and constraints. This simplicity allows the calibration of hyperspectral images with a large number of bands in a reasonable runtime. As in the previous works, we currently calibrate each band separately; however, the model can be easily modified to calibrate all the bands simultaneously including constraints between different bands. The current version of our method considers cases with a small effect of the BRDF that can be ignored in the model and minimized due to the applied constraints. Adaptation to cases with high influence of the BRDF will be considered in our future works. Finally, using an automatic method for tie point extraction, specifically the *scale-invariant feature transform* (SIFT) method [36], our method can be applied to sets with different data types from different sensors.

We provide a new *generalized empirical line* (GEL) model that allows calibration of multiple images simultaneously with an option to introduce constraints on the obtained fractions. The proposed GEL is hybrid and allows easy selection from four modes. Each mode is suitable for different cases considering the number of images, single or multiple, and the option of constrained or unconstrained calibration:

1) EL for traditional EL calibration of single image;
2) *multiple image empirical line* (MIEL) for simultaneous unconstrained calibration of bundle of images;
3) *constrained empirical line* (CEL) for constrained EL calibration of a single image;
4) *multiple image constrained empirical line* (MIcEL) for simultaneous constrained calibration of bundle of images.

The rest of this paper is organized as follows. Section II presents the methodology of the proposed work and the concepts of the GEL model, including detailed description of the calibration framework components and the needed analytical

formulations. Section III presents an experimental performance evaluation of the proposed EL, CEL, MIEL, and MIcEL, with comparison to QUAC. Finally, Section IV presents the discussion and conclusions.

II. Methodology and Concepts of the GEL Model

A. Basic EL Calibration Model

Assuming a simplified linear relationship between the DN of a given pixel and the corresponding reflectance value, the basic EL model is given by

$$\rho_\lambda = a_\lambda \cdot \mathrm{DN}_\lambda + b_\lambda \tag{1}$$

where ρ_λ is the reflectance value at wavelength λ, DN_λ is the DN in the corresponding spectral band, and a_λ and b_λ are the calibration coefficients representing the slope and intercept of a straight line, respectively. Accordingly, to calibrate the entire image, a pair of calibration coefficients a_λ and $b_\lambda$is estimated for each band in the image using the reflectance values of reference/ground targets that can be easily recognized in the image. Usually, a dark target (low reflectance value) and bright target (high reflectance value) are assumed to span the range of the obtained reflectance values, therefore, they are preferred to be used as ground targets in the calibration.

B. GEL Model for Simultaneous Calibration of Multiple Images

Let us consider a set of s spectral images $\mathbf{I} = \{\mathbf{I}^1, \mathbf{I}^2, \ldots, \mathbf{I}^s\}$ acquired on an area of interest, where each image has a partial spatial overlapping with at least one other image (see Fig. 1). Let us assume that ground targets exist, which can be recognized, in one or more images and their reflectance values are available by laboratory or spectroradiometer field measurements. We can calibrate the entire set of images $\mathbf{I}$ using the ground targets and tie points (pixels) that appear in the overlapping area between two or more images (see Fig. 1). For this purpose, we use the basic EL model and define two different types of equations that map DN values to reflectance values.

Let $\mathbf{I}^k(x_i, y_i, \lambda)$ denote the DN value of the ith ground target point (a point within ground target), located on (x_i, y_i), as measured in the spectral band corresponding to the wavelength λ in the image $\mathbf{I}^k$. Let a_λ^k and b_λ^k denote the calibration coefficients for this band. We define the first type of equation based on mapping the DN to reflectance based on using ground target points. Each point provides one equation, according to (1), as follows:

$$\rho_\lambda^i = a_\lambda^k \cdot \mathbf{I}^k(x_i, y_i, \lambda) + b_\lambda^k \tag{2}$$

where ρ_λ^i is the reflectance value of the ith ground target point at wavelength λ.

Accordingly, let $\mathbf{I}^l$ and $\mathbf{I}^r$ be a pair of partially overlapped images, and let $\mathbf{I}^l(x_j, y_j, \lambda)$ and $\mathbf{I}^r(x_j, y_j, \lambda)$ denote the DN values of the jth tie point, located on (x_j, y_j), as measured in the spectral band corresponding to the wavelength λ in $\mathbf{I}^l$ and $\mathbf{I}^r$, respectively. We define a second type of equation based on mapping the DN of one image to reflectance through the DN of neighbor image using tie points. Each tie point provides one equation

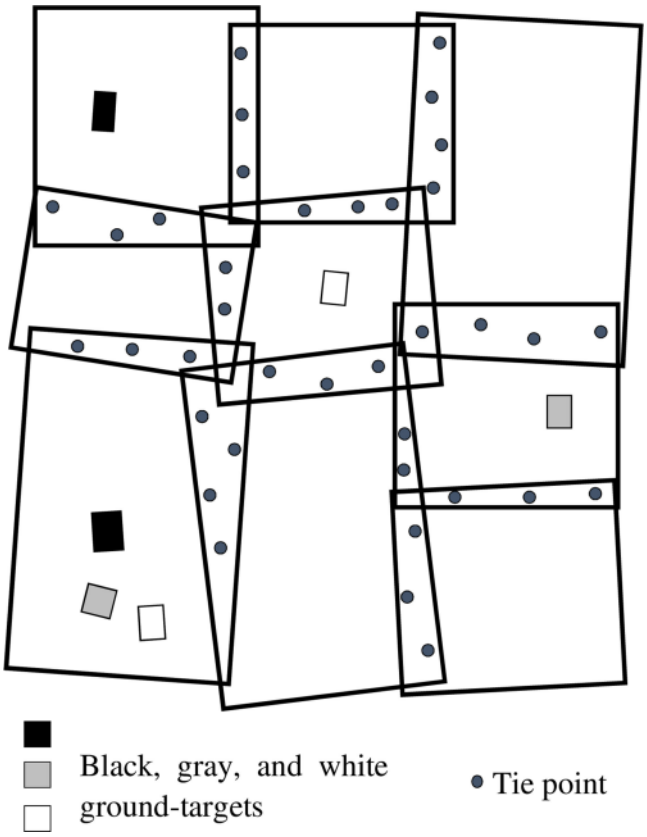

Fig. 1. Conceptual scheme of a set of partially overlapping images with the presence of ground targets.

$$\rho_\lambda^j = a_\lambda^r \cdot \mathbf{I}^r(x_j, y_j, \lambda) + b_\lambda^r. \tag{3}$$

In practice, the reflectance value of the jth tie point ρ_λ^j is not available in this stage. However, recall that this tie point is recognized also in the image $\mathbf{I}^l$, and according to (1), we can assign $\rho_\lambda^j = a_\lambda^l \cdot \mathbf{I}^l(x_j, y_j, \lambda) + b_\lambda^l$ in (3) to obtain the following:

$$a_\lambda^l \cdot \mathbf{I}^l(x_j, y_j, \lambda) + b_\lambda^l = a_\lambda^r \cdot \mathbf{I}^r(x_j, y_j, \lambda) + b_\lambda^r. \tag{4}$$

Finally, we can formulate the second-type equation as

$$a_\lambda^r \cdot \mathbf{I}^r(x_j, y_j, \lambda) + b_\lambda^r - a_\lambda^l \cdot \mathbf{I}^l(x_j, y_j, \lambda) - b_\lambda^l = 0. \tag{5}$$

Then, given n ground target points located on $\{(x_1, y_1), (x_2, y_2), \ldots, (x_n, y_n)\}$ and m tie points located on $\{(x_{n+1}, y_{n+1}), (x_{n+2}, y_{n+2}), \ldots, (x_{n+m}, y_{n+m})\}$, we can construct a system of $(n+m)$ linear equations. Let $\mathbf{I}^{k_i}$ denote an image where the ith ground target point can be recognized, and $\mathbf{I}^{r_j}$ and $\mathbf{I}^{l_j}$ denote a pair of images where the jth tie point can be recognized. Then, the system of linear equations, L, can be written as the first equation at the bottom of the next page, and in matrix form as

$$\mathbf{D}\mathbf{x} = \mathbf{d} \tag{6}$$

where $\mathbf{x}$ is the vector of unknowns, i.e., the calibration coefficients of all the images, which is given by

$$\mathbf{x} = \left[a_\lambda^1, b_\lambda^1, a_\lambda^2, b_\lambda^2, \ldots, a_\lambda^s, b_\lambda^s\right]^T \tag{7}$$

and $\mathbf{D}$ is the matrix of partial derivatives with respect to the unknowns. Let L_i denotes the ith linear equation in L, $\mathbf{D}$ is given by (8) as shown bottom of the page.

Let f_1 denotes a first-type equation as in (2), the derivatives of f_1 with respect to the calibration coefficients of the image $\mathbf{I}^k$ are $\frac{\partial f_1}{a_\lambda^k} = \mathbf{I}^k(x_i, y_i, \lambda)$ and $\frac{\partial f_1}{\partial b_\lambda^k} = 1$. For example, let us assume that the first and the second ground target points can be recognized in the first and the third images, respectively. Then, the corresponding rows in $\mathbf{D}$ (row 1 and 2 in this case) will be defined as

$$\begin{bmatrix} \mathbf{I}^1(x_1, y_1, \lambda) & 1 & 0 & 0 & \dots & & & 0 & 0 \\ 0 & 0 & 0 & 0 & \mathbf{I}^3(x_2, y_2, \lambda) & 1 & \dots & 0 & 0 \end{bmatrix}.$$

Accordingly, let f_2 denotes a second-type equation as in (5), the derivatives of f_2 with respect to the calibration coefficients of the first image $\mathbf{I}^l$ are $\frac{\partial f_2}{a_\lambda^l} = -\mathbf{I}^l(x_j, y_j, \lambda)$ and $\frac{\partial f_2}{b_\lambda^l} = -1$, and with respect to the calibration coefficients of the second image $\mathbf{I}^r$ are $\frac{\partial f_2}{a_\lambda^r} = \mathbf{I}^r(x_j, y_j, \lambda)$ and $\frac{\partial f_2}{b_\lambda^r} = 1$.

For example, let us assume that the first tie point can be recognized in both the second and fourth images, the corresponding row in $\mathbf{D}$ (row $(n+1)$ in this case) will be as follows:

$$\begin{bmatrix} 0 & 0 & -\mathbf{I}^2(x_{n+1}, y_{n+1}, \lambda) & -1 & 0 & 0 & \mathbf{I}^4(x_{n+1}, y_{n+1}, \lambda) & 1 & \dots & 0 & 0 \end{bmatrix}.$$

Finally, $\mathbf{d}$ is vector of the right-hand side values of the set of linear equations in L, which for the described case is given by

$$\underset{(n+m)\times 1}{\mathbf{d}} = \begin{bmatrix} \rho_\lambda^1, \dots & \rho_\lambda^n, 0 \dots & 0 \end{bmatrix}^T. \tag{9}$$

Unconstrained estimation of the vector of unknowns can be obtained by solving the following optimization problem:

$$\hat{\mathbf{x}} = \min_{\mathbf{x}} \frac{1}{2} \|\mathbf{D}\mathbf{x} - \mathbf{d}\|_2^2. \tag{10}$$

The described methodology is general and technically applicable to any number of images. However, as in the traditional EL calibration, negative and larger-than-one values are still probable.

To achieve a valid reflectance, with bounded values between zero and one, (i.e., $0 \le \rho \le 1$), we should define the optimization problem in (10) to be constrained as follows:

$$\begin{aligned} \hat{\mathbf{x}} &= \min_{\mathbf{x}} \frac{1}{2} \|\mathbf{D}\mathbf{x} - \mathbf{d}\|_2^2 \\ &\text{s.t.} \\ &\mathbf{A}\mathbf{x} \le \mathbf{c}. \end{aligned} \tag{11}$$

The term $\mathbf{A}\mathbf{x} \le \mathbf{c}$ represents the constraints (as function of the estimated coefficients) for all the pixels in all the images in the set. Each pixel must fulfill two constraints as follows.

Let $\mathbf{I}^k(x_i, y_i, \lambda)$ be the DN of the ith pixels out of p^k pixels in the kth image at the spectral band corresponding to the wavelength λ. We require that $0 \le a_\lambda^k \mathbf{I}^k(x_i, y_i, \lambda) + b_\lambda^k \le 1$, which can be written in a split form as

$$\begin{cases} a_\lambda^k \mathbf{I}^k(x_i, y_i, \lambda) + b_\lambda^k \le 1 \\ -a_\lambda^k \mathbf{I}^k(x_i, y_i, \lambda) - b_\lambda^k \le 0. \end{cases} \tag{12}$$

Applying two constraints for each pixel in the image, as in (12), the number of overall constraints can be very large. On the other hand, using automatic extraction methods, the number of available tie points can be also very large. In practice, this large number of constraints and tie points can be redundant and increases the optimization process complexity without any contribution to the accuracy of the results. To increase the efficiency of our proposed method, we optimize the number of inequality constraint and tie point equations while still using the entire amount of available information.

$$L = \begin{Bmatrix} a_\lambda^{k_1} \cdot \mathbf{I}^{k_1}(x_1, y_1, \lambda) + b_\lambda^{k_1} & = & \rho_\lambda^1 \\ \vdots & & \vdots \\ a_\lambda^{k_n} \cdot \mathbf{I}^{k_n}(x_n, y_n, \lambda) + b_\lambda^{k_n} & = & \rho_\lambda^n \\ a_\lambda^{r_{n+1}} \cdot \mathbf{I}^{r_{n+1}}(x_{n+1}, y_{n+1}, \lambda) + b_\lambda^{r_{n+1}} - a_\lambda^{l_{n+1}} \cdot \mathbf{I}^{l_{n+1}}(x_{n+1}, y_{n+1}, \lambda) - b_\lambda^{l_{n+1}} & = & 0 \\ \vdots & & \vdots \\ a_\lambda^{r_{n+m}} \cdot \mathbf{I}^{r_{n+m}}(x_{n+m}, y_{n+m}, \lambda) + b_\lambda^{r_{n+m}} - a_\lambda^{l_{n+m}} \cdot \mathbf{I}^{l_{n+m}}(x_{n+m}, y_{n+m}, \lambda) - b_\lambda^{l_{n+m}} & = & 0 \end{Bmatrix}$$

$$\mathbf{D} = \begin{bmatrix} \frac{\partial L_1}{\partial a_\lambda^1}, & \frac{\partial L_1}{\partial b_\lambda^1}, & \frac{\partial L_1}{\partial a_\lambda^2}, & \frac{\partial L_1}{\partial b_\lambda^2}, & \dots & \frac{\partial L_1}{\partial a_\lambda^s}, & \frac{\partial L_1}{\partial b_\lambda^s} \\ \frac{\partial L_2}{\partial a_\lambda^1}, & \frac{\partial L_2}{\partial b_\lambda^1}, & \frac{\partial L_2}{\partial a_\lambda^2}, & \frac{\partial L_2}{\partial b_\lambda^2}, & & \frac{\partial L_2}{\partial a_\lambda^s}, & \frac{\partial L_2}{\partial b_\lambda^s} \\ \vdots & & & & \ddots & & \vdots \\ \frac{\partial L_{(n+m)}}{\partial a_\lambda^1}, & \frac{\partial L_{(n+m)}}{\partial b_\lambda^1}, & \frac{\partial L_{(n+m)}}{\partial a_\lambda^2}, & \frac{\partial L_{(n+m)}}{\partial b_\lambda^2}, & \dots & \frac{\partial L_{(n+m)}}{\partial a_\lambda^s}, & \frac{\partial L_{(n+m)}}{\partial b_\lambda^s} \end{bmatrix} \tag{8}$$

C. Optimizing the Number of Inequality Constraints

Considering real hyperspectral scenes, we can reduce the number of constraints to only two for each image. We assume that $0 \leq \mathrm{DN}$ for each pixel in the image, and that DN and ρ are positively correlated, i.e., $0 < a$. Under these assumptions, and considering the linear calibration, pixels with the minimal and maximal values of DN will gain the minimal and maximal values of reflectance in the calibrated band, respectively.

Now, let $\mathbf{I}^k_{(\lambda)\max} = \max\{\mathbf{I}^k(x,y,\lambda)\}$ and $\mathbf{I}^k_{(\lambda)\min} = \min\{\mathbf{I}^k(x,y,\lambda)\}$ be the maximal and minimal DN values in the spectral band λ of the image $\mathbf{I}^k$, respectively. And let a^k_λ and b^k_λ be the calibration coefficients for this band. The reflectance values for this image can be bounded between zero and one, i.e., $0 \leq \rho \leq 1$, by applying the following two constraints:

$$a^k_\lambda \mathbf{I}^k_{(\lambda)\max} + b^k_\lambda \leq 1 \tag{13}$$

$$-a^k_\lambda \mathbf{I}^k_{(\lambda)\,\min} - b^k_\lambda \leq 0. \tag{14}$$

Thus, the partial derivative of the constraints, in (13) and (14), with respect to the calibration coefficients of the image $\mathbf{I}^k$, are $[\,\mathbf{I}^k_{(\lambda)\max}\ 1\,]$ and $[\,-\mathbf{I}^k_{(\lambda)\,\min}\ -1\,]$, respectively. The general matrix of the derivatives of the constraints with respect to the unknowns will then be given by

$$\underset{2s\times 2s}{\mathbf{A}} = \begin{bmatrix} \mathbf{I}^1_{(\lambda)\max} & 1 & 0 & 0 & \dots & 0 & 0 \\ 0 & 0 & \mathbf{I}^2_{(\lambda)\max} & 1 & \dots & 0 & 0 \\ \vdots & \vdots & \vdots & \vdots & \ddots & \vdots & \vdots \\ 0 & 0 & 0 & 0 & \dots & \mathbf{I}^s_{(\lambda)\max} & 1 \\ -\mathbf{I}^1_{(\lambda)\min} & -1 & 0 & 0 & \dots & 0 & 0 \\ 0 & 0 & -\mathbf{I}^2_{(\lambda)\min} & -1 & \dots & 0 & 0 \\ \vdots & \vdots & \vdots & \vdots & \ddots & \vdots & \vdots \\ 0 & 0 & 0 & 0 & \dots & -\mathbf{I}^s_{(\lambda)\min} & -1 \end{bmatrix}.$$

Finally, vector $\mathbf{c}$ composites the corresponding right-hand side values of the constraints, i.e.,

$$\mathbf{c} = \begin{bmatrix} \underset{s\times 1}{\mathbf{1}} \\ \underset{s\times 1}{\mathbf{0}} \end{bmatrix} \tag{15}$$

where $\underset{s\times 1}{\mathbf{1}}$ and $\underset{s\times 1}{\mathbf{0}}$ are the column vectors with s elements of ones and zeros, respectively. Constraining the obtained reflectance values between zero and one (i.e., at 100%) represent the general calibration case, in practice, the proposed model allows bounding the results between any other values. Moreover, different bound values can be easily applied for different images. Let $c^k_{(\lambda)\,\max}$ and $c^k_{(\lambda)\,\min}$ be the desired maximal and minimal reflectance values for the spectral band λ in the kth image, respectively, the general form of the vector $\mathbf{c}$ is given by

$$\mathbf{c} = \Big[c^1_{(\lambda)\,\max}, c^2_{(\lambda)\,\max}, \dots, c^s_{(\lambda)\,\max}, c^1_{(\lambda)\,\min}, c^2_{(\lambda)\,\min}, \dots, c^s_{(\lambda)\,\min}\Big]^T.$$

In some cases, outlier values can be registered in the image due to saturated or damaged pixels. Removing outliers is essential to obtain reliable constrained results, i.e., calculation of minimal and maximal DN values should be applied after the elimination of outliers.

Let $\bar{\mathbf{I}}^k_{(\lambda)} = \mathrm{mean}\{\mathbf{I}^k(x,y,\lambda)\}$ and $\sigma_{\mathbf{I}^k_{(\lambda)}} = \mathrm{stdv}\{\mathbf{I}^k(x,y,\lambda)\}$ be the mean and standard deviation (STD) of the DN values in the spectral band λ of the image $\mathbf{I}^k$ respectively, the DN value $\mathbf{I}^k(x_i,y_i,\lambda)$ is considered as an outlier if

$$\left|\mathbf{I}^k(x_i,y_i,\lambda) - \bar{\mathbf{I}}^k_{(\lambda)}\right| > t\cdot\sigma_{\mathbf{I}^k_{(\lambda)}}.$$

The parameter *t* is used to define the distance of outliers from the mean value in units of STD, different values of *t* will provide different results. An optimal value of *t* can automatically be extracted by an optimization process that minimizes the difference between the measured and estimated reflectance values of selected reference pixels (representing reference targets or field measurements). The optimization problem for this purpose can be defined as

$$\hat{t} = \arg\min_t \left\{\sum_{i=1}^{r}\left(\rho^i_\lambda - \hat{\rho}^i_\lambda\left(\hat{t}\right)\right)^2\right\} \tag{16}$$

where r is the number of reference pixels, and ρ^i_λ and $\hat{\rho}^i_\lambda(\hat{t})$ are the measured and estimated reflectance values (as function of $\hat{t}$), respectively. In practice, we need to solve the problem in (11) at each iteration of the optimization problem in (16). In this work, we set the value of *t* empirically, however, an automatic extraction will be considered in future works.

D. Automatic Detection of Tie Points and Optimizing the Number of Tie Point Equations

A minimal number of two tie points (one with high DN value and the other with low value) is required to connect each pair of overlapping images. Additional points can be relevant for a better representation of the linear relationship between the DN values of two overlapping images. The selection of tie points can be manual, but automatic tie point extraction is preferred since it will improve the calibration process significantly in terms of accuracy by adding a large number of reliable tie points. For this purpose, we specifically use the SIFT method. The method is applied together with the *Random sample consensus* (RANSAC) algorithm [37] to each pair of overlapping images to extract and match inlier key points as follows.

1) Local feature extraction: We use the SIFT method to extract local features at each image and compute their descriptors.
2) Feature matching for key point pairing: The second step of SIFT is to match each feature in the first image with the nearest feature in the other image. Matching metrics between two features can be computed as the Euclidian distance or the spectral angle between corresponding descriptors. Point pair with a match distance lower than a predefined threshold is selected as a successful match.

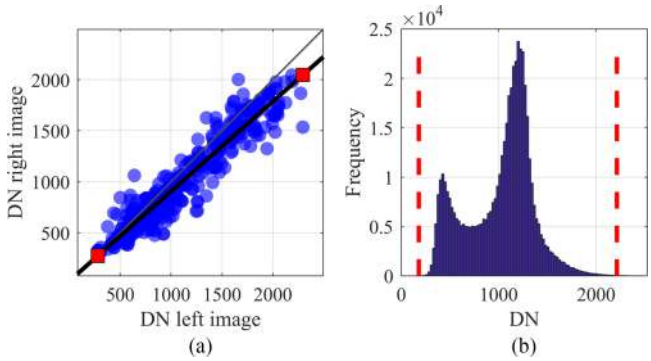

Fig. 2. Illustration of the concepts used to reduce the number of tie point equations and inequality constraints. (a) 2-D scatter plot of measured DN values on matching tie points between pair of overlapping images (blue circles). The black line represents the robust fitted regression line, and the two big red squares on it represent the picked points to be used to construct two tie point equations. Thin straight line represents the 1:1 line. (b) Histogram of DN values in given spectral band, red dashed bars are located on the minimal and maximal DN values after the elimination of outliers. These two values will be used to construct two inequality constrains correspond to this specific image.

3) Filtering outlier: A mismatch in the previous step bears wrong pairs of key points, we use RANSAC to detect and filter these outliers out of the match pairs.

The final corresponding points between each two overlapping images are used to create tie point equations as in (5). The number of extracted tie points by the presented process can be very large. Accordingly, the number of tie point equations will be significantly higher than the number of ground target equations. It is clear that such optimization problem is not efficient. The large number of equations increases the complexity of solving the problem in (11). Moreover, the combination of many tie point equations and only few ground target equations, bears a bias on the obtained solution. The results will probably provide good fitting of the linear relation between the DN of overlapping images but not accurate reflectance values.

One way to overcome this bias is to solve the problem in (11) as a weighted problem, with high weights for ground target equations. However, much more efficient solution can be obtained by reducing the number of needed tie point equations to only two representative equations as follows.

Step 1: We fit a regression line based on the DN values of all the tie pointes between pair of images.

Step 2: We pick two points (one very low and one very high) on the fitted line. These points will be used to construct two tie point equations between this specific pair of images [see Fig. 2(a)]. In addition to the significant reduction of number of equations to be used, this approach allows the use of robust line fitting to reduce the effect of inaccurate tie points.

The concepts of reducing the number of tie points equations and inequality constraints are illustrated in Fig. 2.

An overview of the workflow for simultaneous calibration of a set of multiple overlapping images is presented in Fig. 3. In general, we use ground targets to convert the DN values to reflectance. However, available reflectance images that overlap with at least one of the images to be calibrated can also be used. For this purpose, tie points between the reflectance image and other images will be used to create reflectance equations, i.e., the equation in (3). Moreover, a list of the overlapping image pairs is very useful, if available. Otherwise, such a list can be automatically derived by applying SIFT to all the optional pairs and select those with a feasible number of tie point matches. The main purpose of this part is only to detect the overlapping pairs, thus, for practical reasons, the SIFT algorithm can be applied to low-resolution version of the images.

The problem in (11) represents the general form of the GEL model. In addition to the simultaneous calibration of multiple images under constraints, this model is hybrid and can be easily modified for different modes of calibration (see Fig. 4). The flexibility in the components of the model, in (6)–(15), allows easy selection of different modes to be applied according to the number of images to be calibrated and the need of constrained or unconstrained results.

III. Experimental Evaluation

A comparative testing of the proposed method was carried out with relativity to the QUAC and the standard EL. We use four hyperspectral images with 385 spectral bands (out of 448 after removing noisy and water absorption bands), collected by the AisaFENIX VNIR-SWIR hyperspectral sensor, with spectral range of 350–2500 nm and spatial resolution of ∼2.5 m/pixel. The selected images are subsets of a large dataset that was collected in the project "Environmental mapping and monitoring of Iceland by remote sensing (EMMIRS)" in 2015–2016 [38]. The aerial hyperspectral data were obtained by the Natural Environmental Research Council (http://www.nerc.ac.uk). Image number 1 has an overlapping area with both images number 2 and 4, while image number 2 has an overlapping area with both images number 1 and 3 (see Fig. 5). Three ground targets (with high, medium, and low reflectance properties), each with size of 4×4 m, appear in image number 1 and can be also recognized in image number 2 (see Fig. 5). These targets will be used for calibration and validation. The spectral signatures (reflectance and DN) of the ground targets are presented in Fig. 6. An evaluation of the overall accuracy is carried out with respect to 11 field measurements representing different areas, each with size of 4×4 m. These areas were selected to represent diverse land-cover types, including grassland (point 1), a mixture of grassland and lava rock (points 2 and 3), a mixture of mosses and dwarf shrubs (point 4), a mixture of birch shrubs (*Betula pubescens*) and dwarf shrubs (point 5), gravelly surface with a mixture of lava rock and tephra (point 6), willow shrubs (*Salix phylicifolia*) (point 7), mixture of sedges and mosses (point 8), restored grassland (point 9), cotton grass (*Eriophorum angustifolium*) wetland (point 10), and mixture of grasses and sedges wetland margin (point 11). The reflectance was measured, close in time to the acquisition of the images, using an ASD (www.asdi.com) field spectroradiometer with 2151 spectral bands. Finally, the field spectra were convolved to the spectral response of the 448 bands of the AISA sensor.

Considering this specific case, we need to solve a constrained least squares problem with eight unknowns (two coefficients

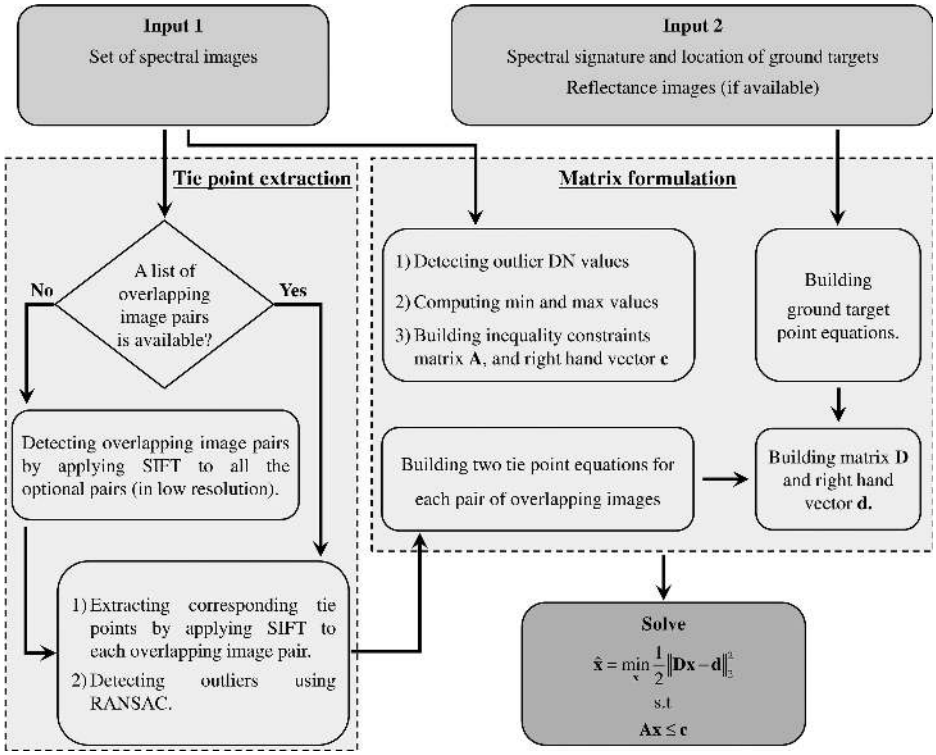

Fig. 3. Workflow for applying the proposed GEL calibration.

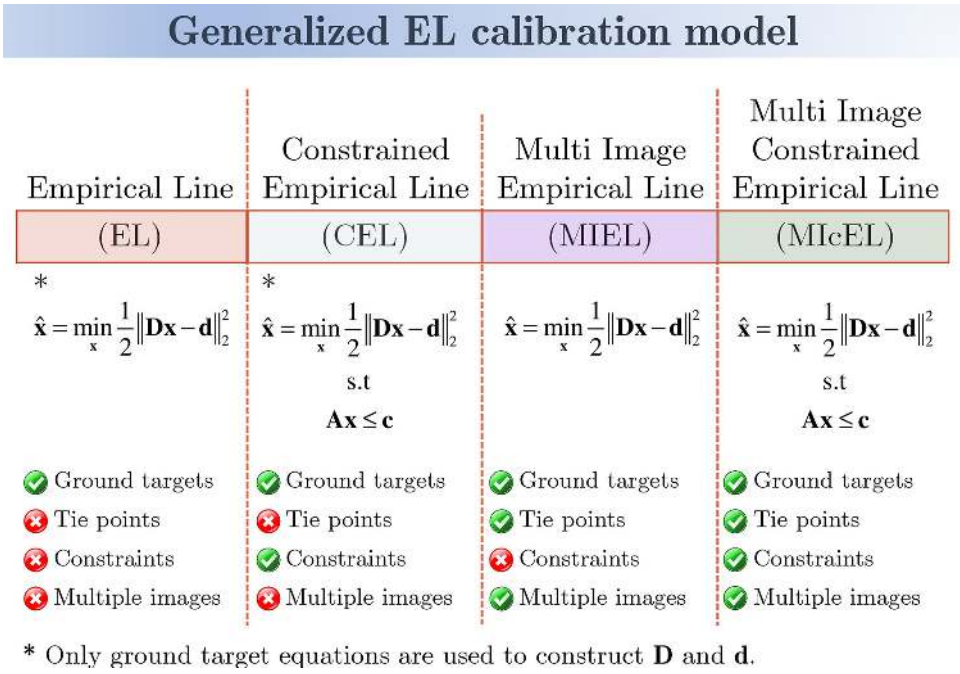

Fig. 4. Four calibration modes available within the proposed generalized EL calibration model. All the modes require ground targets, but vary by the use of tie points, constraints, and applicability for multiple images.

for each image) for each band. The coefficients of each band will be calibrated separately. Using the form of reduced number of equations and constraints, each time we need to solve a constrained least squares problem with nine equations (three correspond to ground targets and six correspond to tie points), and eight inequality constraints (two for each image).

A. Tie Point Extraction

SIFT algorithm detects 374 matching points between images 1 and 2, 64 matching points between images 2 and 3, and 404 matching points between images 1 and 4. Fig. 7 shows the pair of overlapping images 1 and 2 (with plot of connecting

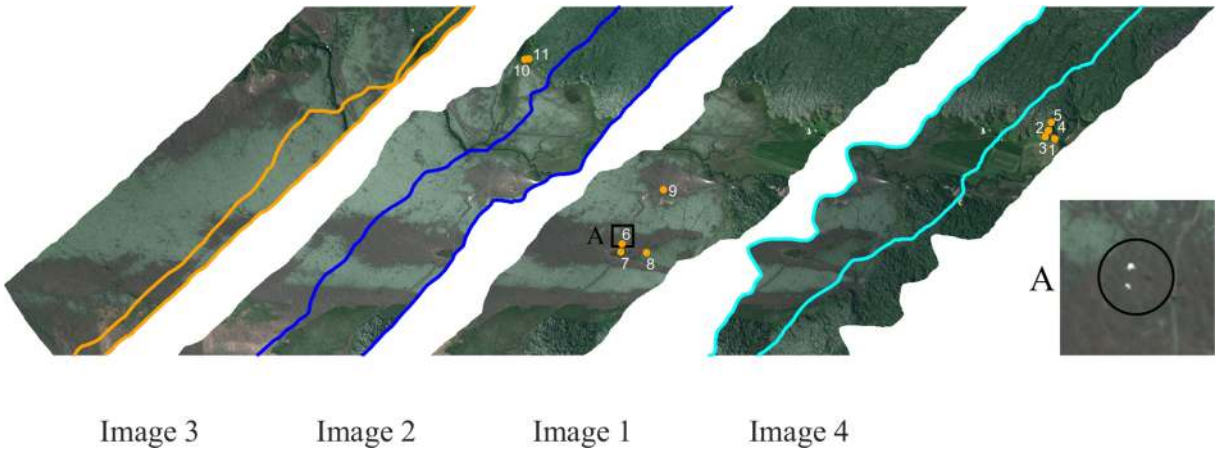

Fig. 5. Four spectral images (strips) used for evaluation of the proposed methodology. Orange, blue, and cyan lines represent the boundaries of the overlapping area between images 2 and 3, images 1 and 2, and images 1 and 4, respectively. The black rectangle area (A) in image number 1 indicates (approximately) the position of three ground targets used for the calibration. A zoom on this area is represented in the lower right corner, where the three targets are surrounded by a black circle. The orange dots represent 11 field measurement points that used for evaluation.

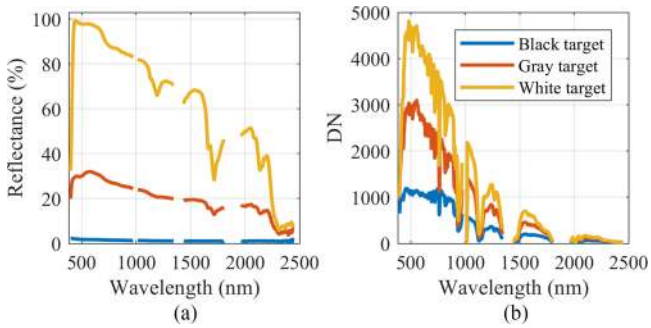

Fig. 6. (a) Mean reflectance values of reference targets measured by field spectroradiometer. (b) Mean DN values of the same reference targets as registered in image number 1.

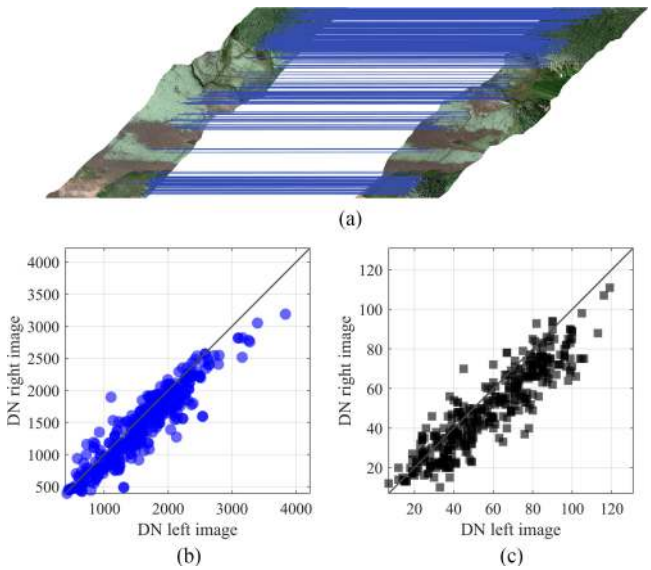

Fig. 7. (a) Pair of images 1 (left) and 2 (right), blue lines connect between matching tie points, (b) and (c) present 2-D scatterplot of left image DN values versus right image DN values in the spectral bands ∼703 and ∼1365 nm, respectively. Dark straight line represents the 1:1 line.

lines between the matching points) and two-dimensional (2-D) scatter plots of DN values on the tie points as registered on the pair of images in two selected spectral bands. Fig. 7 emphasizes the efficiency of the SIFT algorithm for automatic detection of tie points. The 2-D scatterplots show the linear relationship between the DN values of two overlapping images.

B. Accuracy Assessment

For a quantitative assessment of the methods' accuracy, we define the *pixel mean absolute error* (pMAE) between two spectral signatures ρ^1 and ρ^2 as

$$\mathrm{pMAE}\left(\rho^1, \rho^2\right) = 1/q \sum_{i=1}^{l} \left|\rho^1_{\lambda_i} - \rho^2_{\lambda_i}\right| \tag{17}$$

where $\rho^1_{\lambda_i}$ and $\rho^2_{\lambda_i}$ are the reflectance values at wavelength λ_i, as registered in ρ^1 and ρ^2, respectively, and q is the number of spectral bands.

1) Image-to-Image Accuracy: We evaluate the relative image-to-image accuracy by computing the mean absolute error (MAE) between overlapping images. The MAE between two images ($\#k_1$ and $\#k_2$), and its STD, based on tie points, are given by

$$\mathrm{MAE}_{k_1,k_2} = 1/p \sum_{i=1}^{p} \mathrm{pMAE}\left(\hat{\rho}^{i,k_1}, \hat{\rho}^{i,k_2}\right)$$

and

$$\mathrm{STD}\left(\mathrm{MAE}_{k_1,k_2}\right) = \sqrt{1/p \sum_{i=1}^{p} \left(\mathrm{pMAE}\left(\hat{\rho}^{i,k_1}, \hat{\rho}^{i,k_2}\right) - \mathrm{MAE}_{k_1,k_2}\right)^2} \tag{18}$$

where p is the number of tie points, and $\hat{\rho}^{i,k_1}$ and $\hat{\rho}^{i,k_2}$ are the retrieved (estimated) reflectance spectral signatures of the ith tie point as registered in image $\#k_1$ and image $\#k_2$, respectively.

TABLE I
RELATIVE IMAGE-TO-IMAGE MAE (%) AND STD (%) VALUES FOR EL, CEL, MIEL, MICEL, AND QUAC

method	Images 1 and 2		Images 2 and 3		Images 1 and 4	
	MAE	STD	MAE	STD	MAE	STD
EL	15	9				
CEL	4	2				
MIEL	10	7	8	6	14	12
MIcEL	3	2	3	2	4	3
QUAC	6	2	6	4	7	4

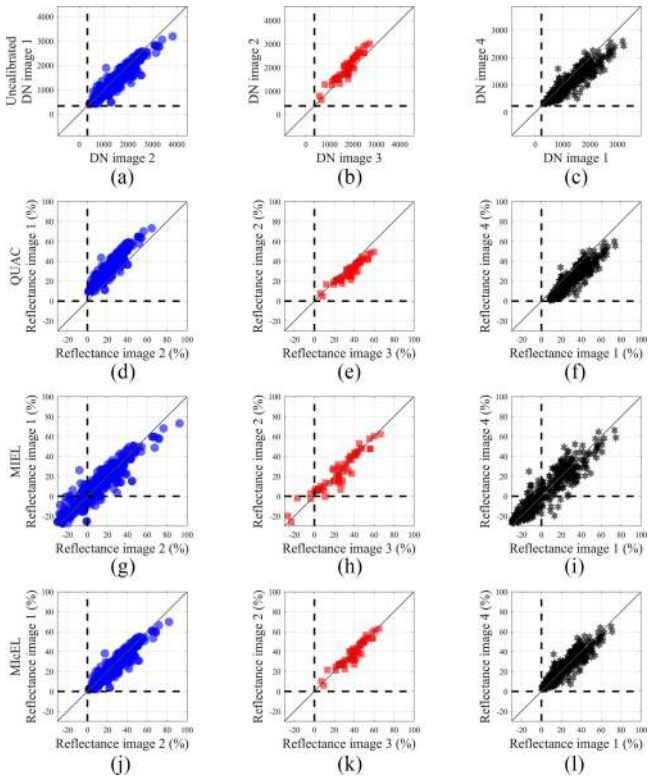

Fig. 8. 2-D scatterplots of data values, in the spectral band ∼703 nm, as registered on tie points between overlapping image pairs, left columns (blue dots) image 1 versus image 2, center columns (red squares) image 2 versus image 3, and right columns (black stars) image 4 versus image 1. Tiles (a), (b), and (c) represent the raw data; (d), (e), and (f) calibrated data by QUAC; (g), (h), and (i) calibrated data by MIEL; and (j), (k), and (l) calibrated data by MIcEL.

Since ground targets are available for both images 1 and 2, we could compute the image-to-image MAE for these images also for the single image calibration methods, EL and CEL. A lower value of the MAE indicates a higher similarity between the reflectance values of same objects that appear in the two images. The results are presented in Table I.

The MAE values clearly show that the obtained results by MIcEL are more accurate than the results obtained by QUAC and by the other calibration modes.

For more insight into the performance of the methods, Fig. 8 shows 2-D scatterplots of the raw and calibrated data, as registered on the tie points between the overlapping image pairs, in the spectral band ∼703 nm. The results of the EL and CEL are available only for the pair of images 1 and 2. In accordance with Table I, the results of EL are similar to those of MIEL, whereas CEL is highly correlated with MIcEL. Therefore, and for convenient presentation, these results are not included in Fig. 8.

TABLE II
PMAE (%) VALUES (PER EACH VALIDATION POINTS) FOR QUAC, MIEL, AND MICEL

Point No'	1	2	3	4	5	6	7	8	9	10	11	mean	STD
QUAC	17	8	12	10	14	7	8	12	8	6	5	**10**	**4**
MIEL	35	37	27	40	35	7	40	36	35	25	23	**31**	**10**
MIcEL	17	10	9	13	14	11	8	13	10	4	10	**11**	**3**

While the obtained results by MIEL are unconstrained (with negative reflectance values in the presented band), both QUAC and MIcEL obtain constrained results with values between 0 and 100%. However, the best-fit line through the MIcEL data cluster is closer to the 1:1 line, i.e., the reflectance values of same objects as appearing in different images are more similar.

2) Overall Accuracy: An assessment of the overall accuracy of QUAC, MIEL, and MIcEL was carried out by computing the pMAE for each of the 11-available validation points by

$$\mathrm{pMAE}_i = \mathrm{pMAE}\left(\rho^i, \hat{\rho}^i\right) \tag{19}$$

where ρ^i and $\hat{\rho}^i$ are the measured (by a field spectroradiometer) and retrieved (estimated) reflectance signatures of the ith validation point, respectively. The results are presented in Table II.

The overall accuracy of the obtained results by MIcEL, with average pMAE of ∼11%, is comparable with respect to the results obtained by QUAC. The noticeable higher accuracy of MIcEL, with respect to MIEL, emphasizes the advantage of applying the constraints in the solution.

3) Image Mosaicking: For a further assessment of the obtained results, by visual analysis, we created a large mosaicked image for each of the methods, QUAC and MIcEL, using the calibrated images. To show the real differences, the mosaic was applied without any color adjustment in the borders between images. The value of pixels in overlapping areas was set as the value of the corresponding pixels in one of the two overlapping images. A mosaicked image of the (normalized) raw data was also created for comparison. Fig. 9 shows an RGB composite of the mosaicked images.

The results in Fig. 9 clearly show the superiority of MIcEL with respect to relative accuracy between overlapping images. The borders of the overlapping areas appear in the mosaic image of the uncalibrated images. These borders are result of different values of the same objects in different images because of the different acquisition conditions and BRDF effect. In accordance with the quantitative results, MIcEL minimizes the differences between values of the same objects in different images. The borders are not noticeable in the MIcEL mosaic image, whereas, some of the borders still clearly noticeable in the QUAC result.

IV. CONCLUSION AND DISCUSSION

In this paper, we present a novel method for the calibration of hyperspectral images. The newly proposed scheme, MIcEL, was developed for constrained and simultaneous calibration of

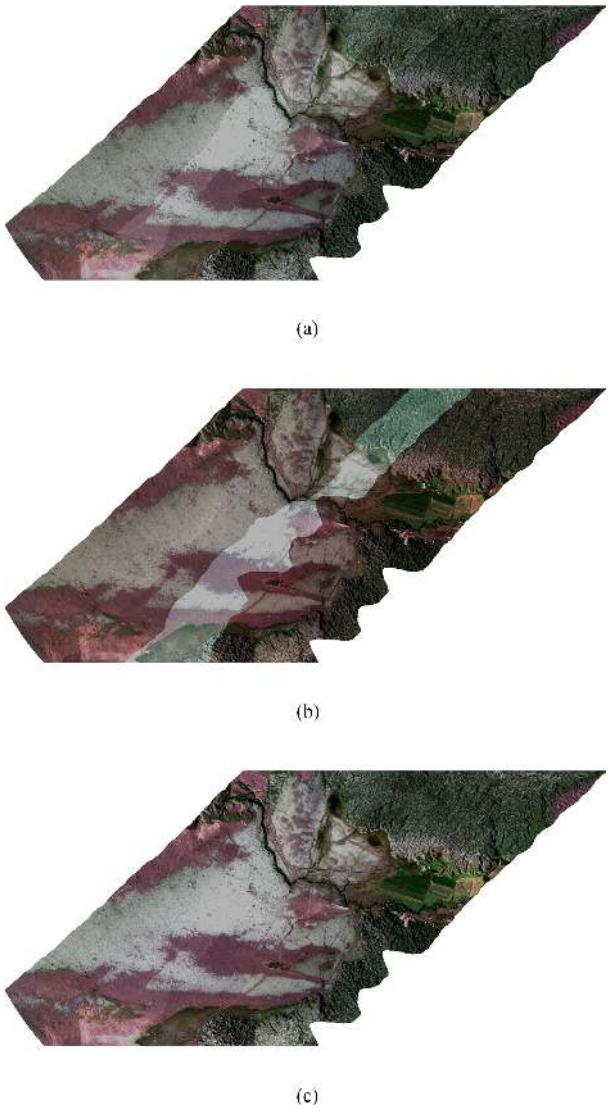

Fig. 9. RGB composition of mosaicked images: (a) original (raw uncalibrated images), (b) calibrated images by QUAC, and (c) calibrated images by MIcEL.

multiple images with partial spatial overlap. However, its hybrid form makes it suitable also for the calibration of single images and allows an easy selection between constrained and unconstrained solutions. We modify the basic EL model to formulate a new GEL model, which can be represented as a simple linear equation system that combines reflectance and tie point equations. Reflectance equations convert *DN* values to absolute reflectance through ground targets, whereas tie point equations are used to optimize the similarity between values of the same objects that appear in different images. Given a set of hyperspectral images with partial overlaps, the newly proposed scheme is used to solve a constrained least squares problem to estimate the absolute calibration coefficients of each image directly. We reduce the data redundancy to optimize the number of tie point equations to only two for each pair of overlapping images, and the number of constraints to two for each image. For example, given a set of s images, to be calibrated using n ground target points, we solve a problem with $n + 2 \times (s - 1)$ equations under $2 \times s$ constraints. Due to its low complexity, the proposed method can be very useful for big imaging campaigns. In addition, using SIFT method for automatic extraction of tie points, the proposed methodology can be applied to datasets that include diverse types of images, from different sensors and with different resolutions. In the current version of the proposed GEL, the BRDF effect is not addressed explicitly. Nevertheless, the results showed that the constraints incorporation helps us to reduce this effect. The empirical results demonstrated the superiority of the MIcEL with respect to image-to-image accuracy, which measures the consistency of the calibrated information of the same objects, in different images. Moreover, the overall absolute accuracy of MIcEL, with respect to field measurements, is comparable with the QUAC method.

As a part of future work, it would be of interest to address the incorporation of the BRDF effect in the GEL. Furthermore, it is worthy to examine the proposed method using big datasets, with many images, and test the error propagation of the calibration, with relativity to the distance from images that contain ground targets. In addition, comparison with RTM-based method (e.g., MODTRAN) will be considered in our future work.

ACKNOWLEDGMENT

The authors would like to thank the Icelandic Research Fund for the partial support of this research through the EMMIRS project. The authors would also like to thank the Associate Editor and the anonymous reviewers for their helpful comments and suggestions.

REFERENCES

[1] G. W. Staben, K. Pfitzner, R. Bartolo, and A. Lucieer, "Empirical line calibration of WorldView-2 satellite imagery to reflectance data: Using quadratic prediction equations," *Remote Sens. Lett.*, vol. 3, no. 6, pp. 521–530, Nov. 2012.

[2] A. Cardesin Moinelo, G. Piccioni, E. Ammannito, G. Filacchione, and P. Drossart, "Calibration of hyperspectral imaging data: VIRTIS-M onboard venus express," *IEEE Trans. Geosci. Remote Sens.*, vol. 48, no. 11, pp. 3941–3950, Nov. 2010.

[3] G. Schaepman-Strub, M. E. Schaepman, T. H. Painter, S. Dangel, and J. V. Martonchik, "Reflectance quantities in optical remote sensing-definitions and case studies," *Remote Sens. Environ.*, vol. 103, no. 1, pp. 27–42, 2006.

[4] S. Collings, P. Caccetta, N. Campbell, and X. Wu, "Techniques for BRDF correction of hyperspectral mosaics," *IEEE Trans. Geosci. Remote Sens.*, vol. 48, no. 10, pp. 3733–3746, Oct. 2010.

[5] P. Poulin and A. Fournier, "A model for anisotropic reflection," *ACM SIGGRAPH Comput. Graph.*, vol. 24, no. 4, pp. 273–282, 1990.

[6] W. Wanner *et al.*, "Global retrieval of bidirectinal reflectance and albedo over land from EOS MODIS and MISR data: Theory and algorithm," *J. Geophys. Res. Atmos.*, vol. 102, no. D14, pp. 17143–17161, 1997.

[7] W. Lucht, C. B. Schaaf, and A. H. Strahler, "An algorithm for the retrieval of albedo from space using semiempirical BRDF models," *IEEE Trans. Geosci. Remote Sens.*, vol. 38, no. 2 II, pp. 977–998, Mar. 2000.

[8] G. Camps-Valls, D. Tuia, L. Bruzzone, and J. A. Benediktsson, "Advances in hyperspectral image classification: Earth monitoring with statistical learning methods," *IEEE Signal Process. Mag.*, vol. 31, no. 1, pp. 45–54, Jan. 2014.

[9] A. Plaza *et al.*, "Recent advances in techniques for hyperspectral image processing," *Remote Sens. Environ.*, vol. 113, no. Suppl. 1, pp. S110–S122, Sep. 2009.

[10] J. M. Bioucas-Dias *et al.*, "Hyperspectral unmixing overview: Geometrical, statistical, and sparse regression-based approaches," *IEEE J. Sel. Topics Appl. Earth Observ. Remote Sens.*, vol. 5, no. 2, pp. 354–379, Apr. 2012.

[11] F. Kizel, M. Shoshany, N. S. Netanyahu, G. Even-Tzur, and J. A. Benediktsson, "A stepwise analytical projected gradient descent search for hyperspectral unmixing and its code vectorization," *IEEE Trans. Geosci. Remote Sens.*, vol. 55, no. 9, pp. 4925–4943, Sep. 2017.
[12] M. T. Eismann, J. Meola, and R. C. Hardie, "Hyperspectral change detection in the presence of diurnal and seasonal variations," *IEEE Trans. Geosci. Remote Sens.*, vol. 46, no. 1, pp. 237–249, Jan. 2008.
[13] R. J. Radke, S. Andra, O. Al-Kofahi, and B. Roysam, "Image change detection algorithms: A systematic survey," *IEEE Trans. Image Process.*, vol. 14, no. 3, pp. 294–307, Mar. 2005.
[14] J. Xu and J. Huang, "Refined empirical line method to calibrate IKONOS imagery," *J. Zhejiang Univ. A*, vol. 7, no. 4, pp. 641–646, Apr. 2006.
[15] A. Berk *et al.*, "MODTRAN cloud and multiple scattering upgrades with application to AVIRIS," *Remote Sens. Environ.*, vol. 65, no. 3, pp. 367–375, 1998.
[16] M. W. Matthew *et al.*, "Atmospheric correction of spectral imagery: Evaluation of the FLAASH algorithm with AVIRIS data," in *Proc. Appl. Imagery Pattern Recognit. Workshop*, Jan. 2002, pp. 157–163.
[17] R. Richter and D. Schläpfer, "Geo-atmospheric processing of airborne imaging spectrometry data. Part 2: Atmospheric/topographic correction," *Int. J. Remote Sens.*, vol. 23, no. 13, pp. 2631–2649, Jan. 2002.
[18] P. S. J. Chávez, "Image-based atmospheric corrections - revisited and improved," *Photogramm. Eng. Remote Sens.*, vol. 62, no. 9, pp. 1025–1036, 1996.
[19] B.-C. Gao, C. Davis, and A. Goetz, "A review of atmospheric correction techniques for hyperspectral remote sensing of land surfaces and ocean color," in *Proc. IEEE Int. Symp. Geosci. Remote Sens.*, 2006, pp. 1979–1981.
[20] L. S. Bernstein, S. M. Adler-Golden, X. Jin, B. Gregor, and R. L. Sundberg, "Quick atmospheric correction (QUAC) code for VNIR-SWIR spectral imagery: Algorithm details," in *Proc. 4th Workshop Hyperspectral Image Signal Process., Evol. Remote Sens.*, 2012, pp. 1–4.
[21] L. S. Bernstein, "Quick atmospheric correction code: Algorithm description and recent upgrades," *Opt. Eng.*, vol. 51, no. 11, 2012, Art. no. 111719.
[22] G. M. Smith and E. J. Milton, "The use of the empirical line method to calibrate remotely sensed data to reflectance," *Int. J. Remote Sens.*, vol. 20, no. 13, pp. 2653–2662, Jan. 1999.
[23] E. Karpouzli and T. Malthus, "The empirical line method for the atmospheric correction of IKONOS imagery," *Int. J. Remote Sens.*, vol. 24, no. 5, pp. 1143–1150, Jan. 2003.
[24] S. Collings, P. Caccetta, N. Campbell, and X. Wu, "Empirical models for radiometric calibration of digital aerial frame mosaics," *IEEE Trans. Geosci. Remote Sens.*, vol. 49, no. 7, pp. 2573–2588, Jul. 2011.
[25] R. Müller, "Calibration and verification of remote sensing instruments and observations," *Remote Sens.*, vol. 6, no. 6, pp. 5692–5695, 2014.
[26] N. Mishra, D. Helder, A. Angal, J. Choi, and X. Xiong, "Absolute calibration of optical satellite sensors using libya 4 pseudo invariant calibration site," *Remote Sens*., vol. 6, no. 2, pp. 1327–1346, 2014.
[27] D. G. Hadjimitsis, C. R. I. Clayton, and A. Retalis, "The use of selected pseudo-invariant targets for the application of atmospheric correction in multi-temporal studies using satellite remotely sensed imagery," *Int. J. Appl. Earth Observ. Geoinf.*, vol. 11, no. 3, pp. 192–200, Jun. 2009.
[28] A. Brook and E. Ben-Dor, "Supervised vicarious calibration (SVC) of multi-source hyperspectral remote-sensing data," *Remote Sens*., vol. 7, no. 5, pp. 6196–6223, 2015.
[29] H. Li, H. Zhang, B. Zhang, Z. Chen, M. Yang, and Y. Zhang, "A method suitable for vicarious calibration of a UAV hyperspectral remote sensor," *IEEE J. Sel. Topics Appl. Earth Observ. Remote Sens.*, vol. 8, no. 6, pp. 3209–3223, Jun. 2015.
[30] J. D. Ortiz *et al.*, "Intercomparison of approaches to the empirical line method for vicarious hyperspectral reflectance calibration," *Front. Mar. Sci.*, vol. 4, 2017, Art. no. 296.
[31] W. M. Baugh and D. P. Groeneveld, "Empirical proof of the empirical line," *Int. J. Remote Sens.*, vol. 29, no. 3, pp. 665–672, 2008.
[32] G. W. Staben, K. Pfitzner, R. Bartolo, and A. Lucieer, "Empirical line calibration of WorldView-2 satellite imagery to reflectance data: Using quadratic prediction equations," *Remote Sens. Lett.*, vol. 3, no. 6, pp. 521–530, 2012.
[33] J. F. Xu and J. F. Huang, "Empirical line method using spectrally stable targets to calibrate IKONOS imagery," *Pedosphere*, vol. 18, no. 1, pp. 124–130, Feb. 2008.
[34] B. Clark, J. Suomalainen, and P. Pellikka, "The selection of appropriate spectrally bright pseudo-invariant ground targets for use in empirical line calibration of SPOT satellite imagery," *ISPRS J. Photogramm. Remote Sens.*, vol. 66, no. 4, pp. 429–445, Jul. 2011.
[35] E. Honkavaara, T. Hakala, L. Markelin, T. Rosnell, H. Saari, and J. Mäkynen, "A process for radiometric correction of UAV image blocks," *Photogramm. - Fernerkundung - Geoinf.*, vol. 2012, no. 2, pp. 115–127, 2012.
[36] D. G. Lowe, "Distinctive image features from scale-invariant keypoints," *Int. J. Comput. Vision*, vol. 60, no. 2, pp. 91–110, Nov. 2004.
[37] M. A. Fischler and R. C. Bolles, "Random sample consensus," *Commun. ACM*, vol. 24, no. 6, pp. 381–395, 1981.
[38] G. B. M. Pedersen *et al.*, "Environmental mapping and monitoring of Iceland by remote sensing (EMMIRS)," in *Proc. EGU Gen. Assem*, Vienna, Austria, Apr. 17–22, 2016, vol. 18, Paper 12432.

Fadi Kizel (M'17) received the M.Sc. and Ph.D. degrees in mapping and geoinformation engineering from the Technion–Israel Institute of Technology, Haifa, Israel, in 2009 and 2014, respectively.

From 2006 to 2014, he was a member with the Environmental Remote Sensing Laboratory Research Group, Technion–Israel Institute of Technology. From 2015 to 2016, he was a Researcher of the CITI-SENSE Project with the Technion Center of Excellence in Exposure Science and Environmental Health, Haifa. He is currently a Postdoctoral Researcher with the Signal Processing Laboratory, Faculty of Electrical and Computer Engineering, University of Iceland, Reykjavík, Iceland. He is also a Researcher of the Environmental Mapping and Monitoring of Iceland by Remote Sensing Project. His research interests include (hyper)spectral image processing and data analysis, with a focus on the spectral unmixing problem.

Dr. Kizel serves as a Reviewer of the IEEE TRANSACTION ON GEOSCIENCE AND REMOTE SENSING, IEEE GEOSCIENCE AND REMOTE SENSING LETTERS, and the IEEE ACCESS.

Jón Atli Benediktsson (S'84–M'90–SM'99–F'04) received the Cand.Sci. degree in electrical engineering from the University of Iceland, Reykjavik, Iceland, in 1984, and the M.S.E.E. and Ph.D. degrees in electrical engineering from Purdue University, West Lafayette, IN, USA, in 1987 and 1990, respectively.

On July 1 2015, he became the President and Rector with the University of Iceland. From 2009 to 2015, he was the Pro Rector of Science and Academic Affairs and Professor for electrical and computer engineering with the University of Iceland. He is a cofounder of the biomedical start-up company Oxymap (www.oxymap.com). His research interests include remote sensing, biomedical analysis of signals, pattern recognition, image processing, and signal processing, and he has published extensively in those fields.

Prof. Benediktsson was the 2011–2012 President of the IEEE Geoscience and Remote Sensing Society (GRSS) and has been on the GRSS AdCom since 2000. He was the Editor-in-Chief for the IEEE TRANSACTIONS ON GEOSCIENCE AND REMOTE SENSING (TGRS) from 2003 to 2008 and has served as an Associate Editor for TGRS since 1999, the IEEE GEOSCIENCE AND REMOTE SENSING LETTERS since 2003, and IEEE ACCESS since 2013. He is on the Editorial Board of the PROCEEDINGS OF THE IEEE, the International Editorial Board of the *International Journal of Image and Data Fusion*, the Editorial Board of *Remote Sensi*ng, and was the Chairman of the Steering Committee of IEEE JOURNAL OF SELECTED TOPICS IN APPLIED EARTH OBSERVATIONS AND REMOTE SENSING in 2007–2010. He is a Fellow of SPIE. He was a member of the 2014 IEEE Fellow Committee. He was the recipient of the Stevan J. Kristof Award from Purdue University in 1991 as outstanding graduate student in remote sensing. He was the recipient of the Icelandic Research Council's Outstanding Young Researcher Award in 1997, he was granted the IEEE Third Millennium Medal in 2000, a corecipient of the University of Iceland's Technology Innovation Award in 2004, the yearly research award from the Engineering Research Institute of the University of Iceland in 2006, the Outstanding Service Award from the IEEE Geoscience and Remote Sensing Society in 2007, and the OECE Award from the School of ECE, Purdue University in 2016. He was a corecipient of the 2012 IEEE Transactions on Geoscience and Remote Sensing Paper Award and the IEEE GRSS Highest Impact Paper Award in 2013. In 2013, he was the recipient of the IEEE/VFI Electrical Engineer of the Year Award. In 2014, he was a corecipient of the International Journal of Image and Data Fusion Best Paper Award. He is a member of the Association of Chartered Engineers in Iceland (VFI), Societas Scinetiarum Islandica, and Tau Beta Pi.

Lorenzo Bruzzone (S'95–M'98–SM'03–F'10) received the Laurea (M.S.) degree in electronic engineering (summa cum laude) and the Ph.D. degree in telecommunications from the University of Genoa, Genoa, Italy, in 1993 and 1998, respectively.

He is currently a Full Professor of telecommunications with the University of Trento, Trento, Italy, where he teaches remote sensing, radar and digital communications. He is the founder and the Director with the Remote Sensing Laboratory, Department of Information Engineering and Computer Science, University of Trento. His current research interests include the areas of remote sensing, radar and SAR, signal processing, machine learning, and pattern recognition. He promotes and supervises research on these topics within the frameworks of many national and international projects. He is the Principal Investigator of many research projects. Among the others, he is the Principal Investigator of the *Radar for Icy Moon Exploration* instrument in the framework of the *JUpiter ICy moons Explorer* mission of the European Space Agency. He has authored (or coauthored) 208 scientific publications in referred international journals (151 in IEEE journals), more than 280 papers in conference proceedings, and 21 book chapters. He is the editor/coeditor of 18 books/conference proceedings and one scientific book. His papers are highly cited, as proven form the total number of citations (more than 21 000) and the value of the h-index (70) (source: Google Scholar).

Dr. Bruzzone was invited as a keynote speaker in more than 30 international conferences and workshops. Since 2009, he is a member of the Administrative Committee of the IEEE Geoscience and Remote Sensing Society (GRSS). He ranked first place in the Student Prize Paper Competition of the 1998 IEEE International Geoscience and Remote Sensing Symposium (IGARSS), Seattle, July 1998. He was the recipient of many international and national honors and awards, including the recent *IEEE GRSS 2015 Outstanding Service Award* and the *2017 IEEE IGARSS Symposium Prize Paper Award*. He was a Guest Coeditor of many special issues of international journals. He is the cofounder of the IEEE International Workshop on the Analysis of Multi-Temporal Remote-Sensing Images (MultiTemp) series and is currently a member of the Permanent Steering Committee of this series of workshops. Since 2003, he has been the Chair of the SPIE Conference on Image and Signal Processing for Remote Sensing. He has been the founder of the IEEE GEOSCIENCE AND REMOTE SENSING MAGAZINE for which he has been the Editor-in-Chief between 2013 and 2017. He is an Associate Editor for the IEEE TRANSACTIONS ON GEOSCIENCE AND REMOTE SENSING. He has been a *Distinguished Speaker* of the IEEE Geoscience and Remote Sensing Society between 2012 and 2016.

Gro B. M. Pedersen received the Ph.D. degree in remote sensing and planetary geology from Aarhus University, Aarhus, Denmark, in 2011.

She was a Visiting Research Fellow with Freie Universität, Germany; with Brown University, USA; and with UNIS, Svalbard, Norway during her graduate studies from 2006 to 2011 and worked as a Research Assistant with Hawaii Volcano Observatory, USA, in 2010. She subsequently specialized in semiautomated mapping techniques during her postdoctoral fellowship with the Nordic Volcanological Center, Iceland from 2011 to 2014 and contributed in 2014–2015 to the monitoring of the Holuhraun eruption, Iceland. She is currently a Postdoctoral Research Fellow with the University of Iceland, Reykjavik, Iceland, where she is the Project Leader of the project "Environmental Mapping and Monitoring of Iceland by Remote Sensing" funded by the Icelandic Grant of Excellence. Her research interest includes lava flow dynamics, ice–volcano interactions, and the applications of photogrammetry, geomorphometry, and semiautomated mapping techniques in volcanic settings.

Dr. Pedersen serves as a Reviewer of the *Journal of Geophysical Research* and *International Journal of Remote Sensing and Planetary Space Science*.

Olga K. Vilmundardóttir received the Ph.D. degree in geography from the University of Iceland, Reykjavik, Iceland, in 2015.

She is currently a Postdoctoral Research Fellow with the University of Iceland and is a Researcher in the project "Environmental Mapping and Monitoring of Iceland by Remote Sensing" funded by the Icelandic Grant of Excellence. From 2005 to 2010, she was a Researcher with the Icelandic Institute of Natural History, working on mapping and defining geothermal vegetation in Iceland and monitoring environmental changes along hydro-electric reservoirs. Her research interests include terrestrial ecosystem development on young surfaces and plant response to burial by tephra fall and eolian deposition.

Dr. Vilmundardóttir serves as a Reviewer for the journal *Plant & Soil*.

Nicola Falco (S'10–M'15) received the B.Sc. and M.Sc. degrees in telecommunication engineering from the University of Trento, Trento, Italy, in 2008 and 2011, respectively. He received the joint Ph.D. degree in electrical and computer engineering from the University of Iceland, Reykjavik, Iceland, and in information and communication technologies from the University of Trento, in 2015.

He is currently a Postdoctoral Fellow with the Earth and Environmental Sciences Area—Lawrence Berkeley National Laboratory, Berkeley, CA, USA. His research interests include remote sensing image analysis and processing with applications in environmental monitoring and climate change. His work concentrates on the development of methodologies for data analysis and information extraction mainly in optical and hyperspectral imagery, spanning multiple disciplines, such as image and signal processing, mathematical morphology, pattern recognition, and machine learning.

Dr. Falco was the recipient of the Recognition of IEEE Geoscience Remote Sensing Letters Best Reviewers in 2013, and the corecipient of the third price in the Student Paper Competition of the 2015 IEEE International Geoscience and Remote Sensing Symposium. He is a referee for several international journals, including IEEE TRANSACTION ON GEOSCIENCE AND REMOTE SENSING, IEEE GEOSCIENCE AND REMOTE SENSING LETTERS, IEEE JOURNAL OF SELECTED TOPIC IN APPLIED EARTH OBSERVATIONS AND REMOTE SENSING, *International Journal of Applied Earth Observation and Geoinformation* (Elsevier), *Pattern Recognition Letters* (Elsevier), *International Journal of Remote Sensing and Remote Sensing Letters* (Taylor & Francis), and *Scientific Reports* (Nature).